Transition to stochasticity in the relativistic and the nonrelativistic versions of a dynamical system

Chronis Polymilis
Department of Physics, University of Athens, Panepistimiopolis, 15783 Zografos, Athens, Greece

Kyriakos Hizanidis
Department of Electrical and Computer Engineering, National Technical University of Athens, Athens 10682, Greece
(Received 12 December 1991; revised manuscript received 10 February 1993)

Issues related to the transition to stochastic relativistic and nonrelativistic motion of electrons in an electromagnetic wave propagating obliquely to a uniform magnetic field, such as stability, structure of the diagrams of characteristics, and the morphology of the bifurcation sequence in the latter, are thoroughly investigated. The spatiotemporal distributions of the electron energies, relativistically and nonrelativistically, are also examined. Major, qualitative, as well as quantitative differences in all aspects related to the transition to stochasticity and energy distribution are found. These dramatic differences lead to the conclusion that, at least as far as stochasticity is concerned, the nonrelativistic approximation is invalid even in the weakest possible relativistic case. However, from the theoretical point of view, the nonrelativistic model investigated here is in itself a very rich dynamical system with unusual behavior.

PACS number(s): 41.75.Fr, 41.75.Ht, 05.45.+b

I. INTRODUCTION

The electromagnetic waves along with confining static or quasistatic magnetic fields play the leading role in charged-particle heating and acceleration in a wide variety of physical systems such as fusion devices, accelerators, and man-made or natural radiation sources. As far as the models used in the past to analyze such systems are concerned, there are many based on coherent waves in a magnetic field [1–3], such as the self-resonant electron-cyclotron linear accelerator [4], or high-energy electrons observed in type-III solar bursts [5].

Recently, theoretical studies concerning the stochastic character of motion in the aforementioned systems, in various circumstances, are gaining ground. An example is the stochasticity induced in the case of an obliquely propagating (with respect to the confining static magnetic field) electromagnetic wave where the presence of many cyclotron resonances is very crucial. Below the stochasticity threshold, the motion in this system is nearly integrable and has been studied both in the nonrelativistic [6] and relativistic [7] cases. Stochastic acceleration of particles in the presence of an obliquely propagating electrostatic wave has also been studied in the nonrelativistic [8] as well as the relativistic cases [9,10].

In all the aforementioned studies, no special attention, if any attention at all, was paid to the intrinsic differences which may exist in a relativistic versus a nonrelativistic treatment, even in the mildly relativistic case. Due to the dramatically different functional form of the Hamiltonians involved in these two cases, one may suspect that qualitative differences, as well as quantitative ones to a lesser degree, are present. These differences could lead to differences in the stochastic behavior. The goal of the present work is to demonstrate, through a practically interesting physical system, that these differences really exist and to investigate their impact not only on the various aspects of the onset of stochasticity, but also on the energetics of the charged particles involved. The final outcome of our study exceeded the most speculative of our initial expectations. However, open questions still remain.

The physical system under consideration is electrons interacting with a single electromagnetic wave that propagates at an angle with respect to a uniform external magnetic field. The wave is considered as circularly polarized in a right-handed fashion. A cold, ambient plasma is assumed to exist with an index of refraction [11], $n^2=1-\omega_e^2/\omega(\omega-\Omega)$. Here, ω_e and Ω are the electron plasma and the rest-mass gyrofrequencies, $(4\pi n_e e^2/m_e)^{1/2}$ and eB_0/m_e, respectively (n_e and m_e are the ambient electron density and rest mass, respectively).

The organization of the paper is as follows: In Sec. II the Hamiltonian formulation, along with the choice of the parameters, are briefly discussed. Emphasis is mainly given to describing the calculation of the limiting curves. In Sec. III the transition to stochasticity is illustrated on the basis of the Poincaré Surfaces of Section that are shown. Section IV is devoted to the energetics of the electron motion involved. In Sec. V the stability of the orbits is investigated and the diagrams of characteristics are presented and discussed. The bifurcation sequence in the diagram of characteristics is thoroughly examined in Sec. VI. Finally, in Sec. VII, our main conclusions and results are systematically summarized.

II. HAMILTONIANS, LIMITING CURVES, AND THE EQUATIONS OF MOTION

The physical system under consideration consists of electrons interacting with a right-handed circularly polarized electromagnetic wave propagating at an angle a with respect to a uniform externally imposed magnetic field $\mathbf{B}=\mathbf{e}_z B_0$. The combined effect of the magnetic field

and the wave is expressed via the magnetic potential **A** which is given by

$$\mathbf{A}=A_0(\mathbf{e}_x \cos a \sin\varphi+\mathbf{e}_y \cos\varphi-\mathbf{e}_z \sin a \sin\varphi)+xB_0e_y \ . \tag{1}$$

The phase φ that enters in Eq. (1) is $\varphi=k_x x+k_z z-\omega t$, $\mathbf{e}_x$, $\mathbf{e}_y$, $\mathbf{e}_z$ are the respective unit vectors along the x, y, z axes, and k_x, k_z are the x and y components of the wave vector **k**.

A. Relativistic case

The relativistic electron dynamics is described by an autonomous Hamiltonian of the form [12]

$$H_{\mathrm{R}}=m_e c^2(\gamma-u_\xi/n_z) \ , \tag{2}$$

where

$$\gamma^2=1+(u_x+\epsilon \cos a \sin\psi)^2+(x+\epsilon\cos\psi)^2 +(u_\xi-\epsilon \sin a \sin\psi)^2 \ . \tag{3}$$

In Eqs. (2) and (3) H_{R} is a constant quantity, $n_z=ck_z/\omega$ is the parallel to the magnetic field refraction index, $\psi=(n_x\chi+n_z\zeta)/K$, and $\epsilon=eA_0/mc^2$ is the normalized wave amplitude. The spatial normalized coordinates χ and ζ are $\Omega x/c$ and $\Omega z_1/c$, respectively, where $K\equiv\Omega/\omega$ is the ratio of the cyclotron frequency (with respect to the electron rest mass) $eB_0/m_e c$ to the frequency of the wave and $z_1=z-\omega t/k_z$. The normalized momenta u_x and u_ξ are p_x/mc and p_z/mc, respectively, where p_x, p_z are the canonical momenta conjugate to x and z_1. The canonical momentum p_y (and so u_y) is a constant of the motion, since its conjugate spatial variable y does not enter in the Hamiltonian, and it is taken as zero. [13].

B. Nonrelativistic case

The nonrelativistic limit of Eq. (2) can be easily obtained directly:

$$H_{\mathrm{NR}}=m_e c^2\{1+[(u_x+\epsilon \cos a \sin\psi)^2+(\chi+\epsilon\cos\psi)^2 +(u_\xi-\epsilon \sin a \sin\psi)^2]/2-u_\xi/n_z\} \ . \tag{4}$$

The constant $m_e c^2$ (rest-mass energy) which enters in Eqs. (2) and (4) will be omitted in the sense that, in the analysis which follows, there will be a convention for the correspondence between the relativistic and nonrelativistic cases of the form $h_{\mathrm{R}}\Longleftrightarrow h_{\mathrm{NR}}+1$ with $h_{\mathrm{R,NR}}=H_{\mathrm{R,NR}}/m_e c^2$. The difference between the functional form of expressions (2) and (3), namely, the radical versus the polynomial dependence upon the conjugate variables, is expected to affect the respective dynamical behavior as we will see later.

C. Equations of motion and the limiting curves

The equations of motion to be numerically integrated can be easily derived from the Hamiltonians, Eqs. (2) and (4). In normalized form, they can be written as follows:

$$\frac{d\chi}{d\tau}=\frac{u_\xi-\epsilon \sin a \sin\psi}{\gamma}-\frac{1}{n_z} \ , \tag{5}$$

$$\frac{d\zeta}{d\tau}=\frac{u_x+\epsilon \cos a \sin\psi}{\gamma} \ , \tag{6}$$

$$\frac{du_x}{d\tau}=\frac{\epsilon n_x}{K\gamma}\mu-\frac{\chi+\epsilon\cos\psi}{\gamma} \ , \tag{7}$$

$$\frac{du_\xi}{d\tau}=\frac{\epsilon n_z}{K\gamma}\mu \ , \tag{8}$$

where $\tau=\Omega t$ and μ is given by

$$\mu=(\chi+\epsilon\cos\psi)\sin\psi+(u_\xi-\epsilon \sin a \sin\psi)\sin a \cos\psi -(u_x+\epsilon \cos a \sin\psi)\cos a \cos\psi \ . \tag{9}$$

These equations apply for the relativistic, as well as for the nonrelativistic case if one sets $\gamma=1$ for the latter.

The numerical data shown in this work are based on the choice $\Omega/2\pi=0.98$ MHz, that is, a choice for the magnetic field $B_0=0.35$ G, and $\omega/2\pi=3$ MHz; the ambient density considered is $n_e=10^2$ cm^{-3} and the values for the normalized Hamiltonians h_{R} and h_{NR} are 1.5 and 0.5, respectively. Numerical experiments have also been performed for several parameter settings. Since the sole aim of this work is to reveal intrinsic differences between the relativistic and the nonrelativistic cases and the volume of the data compiled for the figures shown is large, the present work is solely confined in the aforementioned parameter setting.

The Poincaré surfaces of section (PSS) (χ,u_x), for the dynamical system under consideration, are taken every time $n_z\zeta/K$ assumes the value of a multiple of 2π with the same direction of crossing (i.e., sign of $d\zeta/d\tau$). It is also kept track of for the energy, especially for the time of Poincaré surface crossing. In general, there are closed or open areas on PSS which respectively reflect bounded and unbounded motions. The boundaries of these areas on PSS are the so-called limiting curves. They can be found by checking the conditions for existence of real u_ξ solutions of the defining equations for the Hamiltonians, Eqs. (2) and (4), by setting $n_z\zeta/K=2k\pi$. Since the solution of these equations with respect to u_ξ render quadratic equations, the criteria that will define the limiting curves will be the vanishing of the respective discriminants. For the relativistic case, it can be easily found that the region of motion on the PSS (χ,u_x) is given by

$$u_x\le-\epsilon \cos a \sin(n_x\chi/K)-\delta_{\mathrm{R}}^{1/2} \ , \tag{10}$$

$$u_x\ge-\epsilon \cos a \sin(n_x\chi/K)+\delta_{\mathrm{R}}^{1/2} \ , \tag{11}$$

that is, an open region, with

$$\delta_{\mathrm{R}}=h_{\mathrm{R}}^2-1-\epsilon^2\sin^2 a \sin^2(n_x\chi/K)-[\chi+\epsilon\cos(n_x\chi/K)]^2 -[h_{\mathrm{R}}/n_z+\epsilon \sin a \sin(n_x\chi/K)]^2/(1/n_z^2-1) \ . \tag{12}$$

In cases where $\delta_{\mathrm{R}}\le 0$ there is no limiting curve for the relativistic case and, therefore, the permissible area of the motion is *infinite*. As far as the nonrelativistic case is concerned, it can be similarly found that the limiting curve is given by

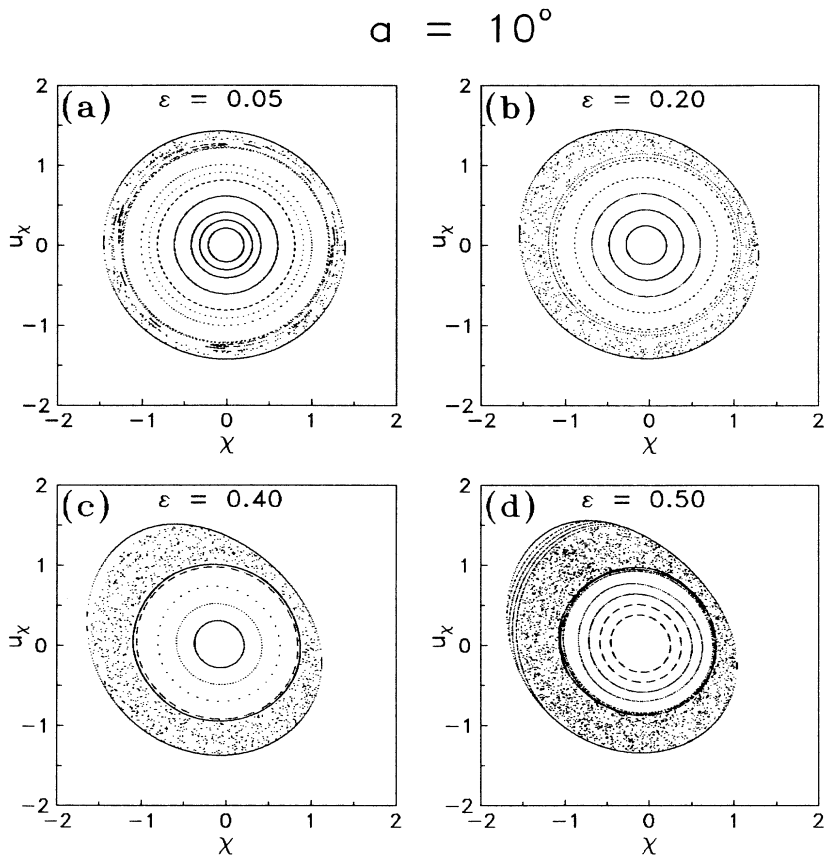

FIG. 1. Nonrelativistic case: Poincaré surfaces of section for propagation angle $a = 10°$ and for normalized amplitude ϵ: (a) 0.05, (b) 0.20, (c) 0.40, and (d) 0.50.

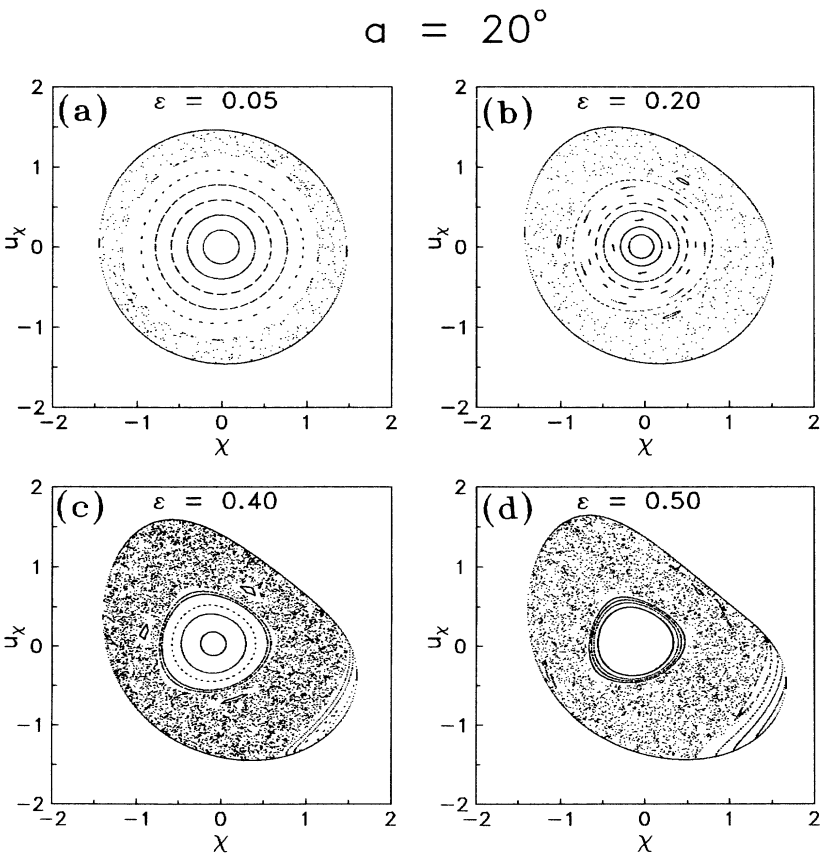

FIG. 2. Nonrelativistic case: Poincaré surfaces of section for propagation angle $a = 20°$ and for normalized amplitude ϵ: (a) 0.05, (b) 0.20, (c) 0.40, and (d) 0.50.

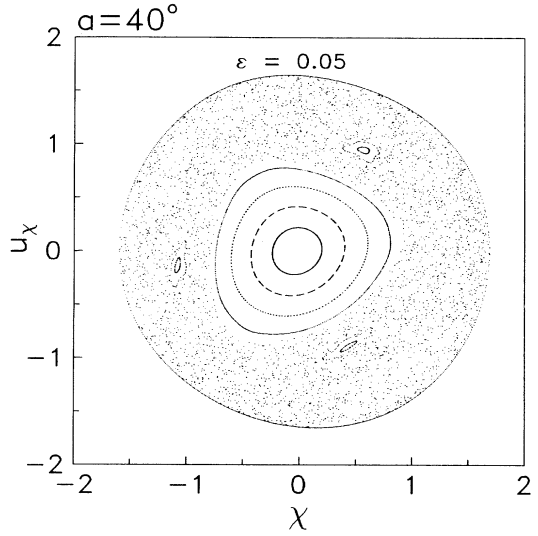

FIG. 3. Nonrelativistic case: Poincaré surfaces of section for propagation angle $a=40°$ and for normalized amplitude $\epsilon=0.05$.

$$-\epsilon\cos a\,\sin(n_x\chi/K)-\delta_{\rm NR}^{1/2}\le u_x\le-\epsilon\cos a\,\sin(n_x\chi/K)+\delta_{\rm NR}^{1/2} \tag{13}$$

with

$$\delta_{\rm NR}=2h_{\rm NR}+\frac{1}{n_z^2}+2\frac{\epsilon}{n_z}\sin a\,\sin(n_x\chi/K)-[\chi+\epsilon\cos(n_x\chi/K)]^2\ . \tag{14}$$

From Eqs. (13) and (14) it is evident that the motion in the nonrelativistic case is a bounded motion. Furthermore, in some cases, the motion can be confined in two or more disjoint areas on the PSS plane.

III. TRANSITION TO STOCHASTICITY

In this section we investigate the various issues related to the onset of stochasticity and its transition rate, such as the extent of the nonstochastic region and its dependence on the values of the propagation angle, a, and the normalized amplitude ϵ. The PSS are taken for several cases for both the relativistic and nonrelativistic models. For the latter we are going to refer to Figs. 1–3 which include solely PSS results, while for the former reference will be made to Figs. 4–13 which, apart from PSS results, include energy consideration results that are discussed in the respective section. The results will be then contrasted in a quantitative manner in Figs. 14 and 15.

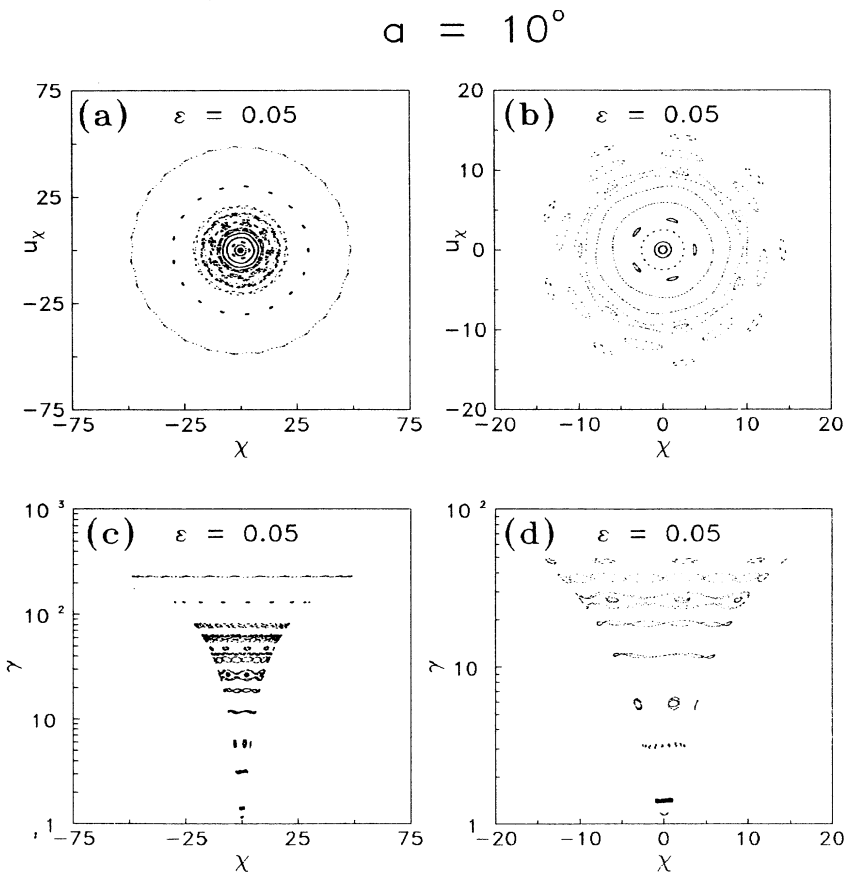

FIG. 4. Relativistic case: Poincaré surfaces of section [(a) and (b)] and total energy, γ, vs normalized position, χ, diagrams [(c) and (d)] for propagation angle $a=10°$ and for normalized amplitude $\epsilon=0.05$. (b) and (d) are fine detail of (a) and (c), respectively.

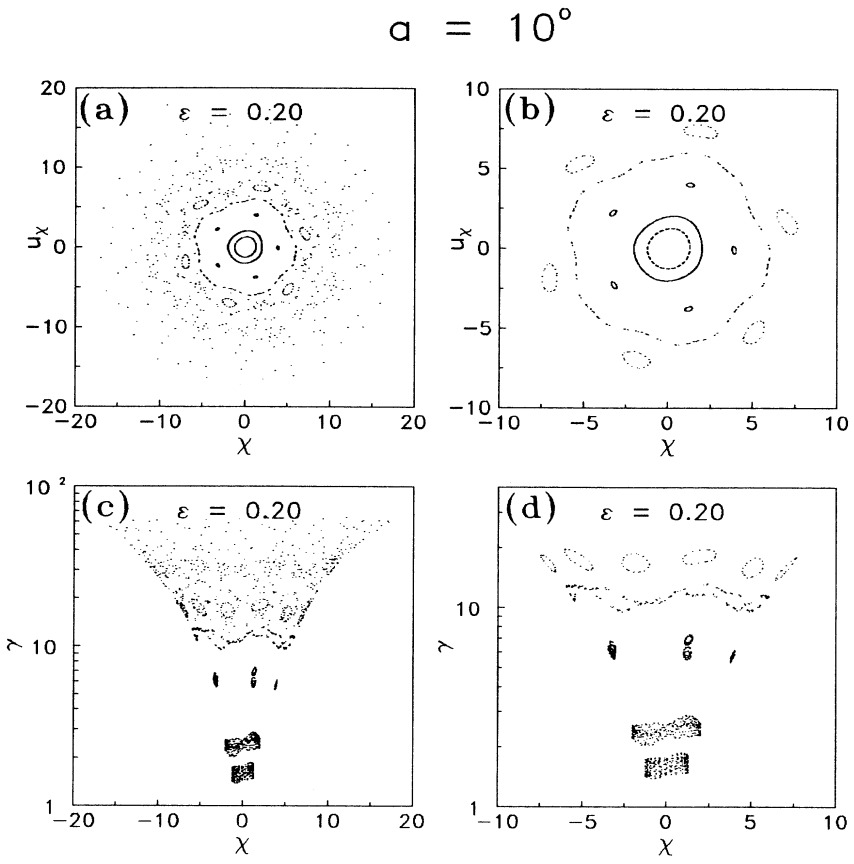

FIG. 5. Relativistic case: Poincaré surfaces of section [(a) and (b)] and total energy, γ, vs normalized position, χ, diagrams [(c) and (d)] for propagation angle $a=10°$ and for normalized amplitude $\epsilon=0.20$. (b) and (d) are fine detail of (a) and (c), respectively.

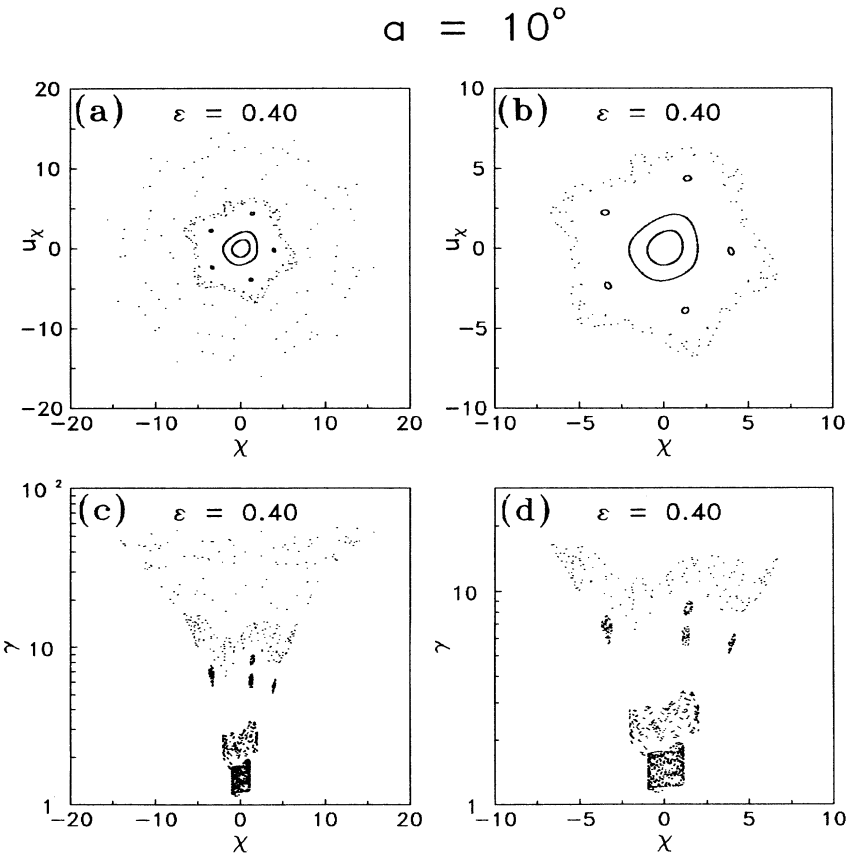

FIG. 6. Relativistic case: Poincaré surfaces of section [(a) and (b)] and total energy, γ, vs normalized position, χ, diagrams [(c) and (d)] for propagation angle $a=10°$ and for normalized amplitude $\epsilon=0.40$. (b) and (d) are fine detail of (a) and (c), respectively.

For the nonrelativistic case the numerical integration time is in the range $\tau=1000-7000$ and the time step $\Delta\tau=0.01-0.05$. In Fig. 1 PSS are shown for propagation angle $a=10°$ and progressively greater values of the normalized amplitude ϵ. The orbits are confined inside the limiting curve which consists of the boundary points in the figures shown. It is clear that for small values of ϵ, the stochastic region is limited and more or less confined in a domain between the limiting curve and regions where the quantity $u_{x0}^2+\chi_0^2$ attains large values. However, as the normalized amplitude increases, the stochastic region increases squeezing in the region of regular motion. For relatively high values of ϵ an isolated "pocket" of organized motion adjacent to the limiting curve appears. This effect can only be explained through stability and bifurcation analysis (Secs. V and VI) and, therefore, for the time being it is left to be discussed later.

In Fig. 2 PSS are shown for propagation angle $a=20°$. Inside the stochastic regions there exist subregions (islands) where the motion is regular; these islands are the so-called "resonances" (existing, though not visible, in Fig. 1 also). By contrasting Figs. 1 and 2 one can readily observe the considerable enlargement of the stochastic region in the latter for the same values of the normalized amplitude ϵ. The isolated "pocket" of regular motion appears again though at lower values of ϵ. It is also evident that the deformation of the limiting curve, as ϵ increases, is more pronounced at higher values of a. Finally, for $a=40°$, the stochastic region is already very wide for small values of ϵ (Fig. 3). For values of ϵ higher than 0.05 almost the whole region inside the limiting curve becomes stochastic. At higher values of a ($a>40°$) there is a clear tendency for the well-developed stochasticity to occur at progressively lower values of ϵ.

Moving now to the relativistic case, in Figs. 4(b), 5(a), 6(a), and 7(a) PSS are shown for $a=10°$ and for four different values of the normalized amplitude, i.e., 0.05, 0.20, 0.40, and 0.50 (the second rows, in these figures, are discussed in Sec. IV). The integration time is in the range $\tau=1000-5000$, the time step $\Delta\tau=0.01-0.05$. It is evident that, as expected, high-order islands (resonances) come and go (being destroyed) as ϵ increases. At the same time, the stochastic region (being unbounded in the relativistic case) increases rapidly. This becomes more evident if one contrasts Figs. 4(a) and 6(a), for instance.

In Figs. 8(a)–11(a) PSS are shown for $a=20°$ and for four values of ϵ (0.05, 0.20, 0.40, and 0.50, respectively). It is clear from Fig. 8 (*vis-à-vis* the $a=10°$ case) that high-order resonances have been moved closer to the origin (by contrasting, for instance, the position of the five islands in their respective figures). Furthermore, at $\epsilon=0.20$ (in Fig. 9, where the regular orbits shown are the last ones in the outward sense), apart from a stable region around $(u_{x0}^2+\chi_0^2)^{1/2}\approx 3$, most of the orbits turn stochastic [compared with Fig. 5(b), for instance]. In Figs. 12(a) and 13(a) finally, PSS are shown for $a=40°$ and 60°, respectively. At higher values of the normalized amplitude, the stochastic orbits visit remote regions on the χ-u_x plane much more frequently and, thus, the stochastic region appears very wide. By contrasting Figs. 4(b) and 13(a) one can easily see (within the same χ-u_x window of observation) that the stochastic region at $a=60°$ extends inwards to lower values of $u_{x0}^2+\chi_0^2$.

The first qualitative conclusion that comes out by contrasting the PSS of the relativistic and nonrelativistic cases is the following: The rate of increase with ϵ of the stochastic region is much more pronounced in the relativistic case. This has also been confirmed by contrasting the times between successive consequents for a stochastic orbit (from the numerical data). This time fluctuates considerably; however, the average period increases much more rapidly with ϵ in the relativistic case than it does in the nonrelativistic one. Long crossing times imply crossing points on a PSS plane far from the center $\chi_0=u_{x0}=0$, and, thus, a wider stochastic region. Therefore, the stochastic transition is much faster in the relativistic case; however, the width of the region for regular motion is much wider in the relativistic case than the one in the nonrelativistic one. Escape has not been observed in the relativistic case, at least for integration times below 200 000 and spatial initial positions below $\chi_0=20$.

In an effort to quantify the onset of stochasticity as the coupling parameter ϵ increases, one faces the problem put by the intrinsic difference between the relativistic and nonrelativistic cases, namely, the unbound character of motion in the former. In the nonrelativistic case it is possible to define the total area of the domain of motion,

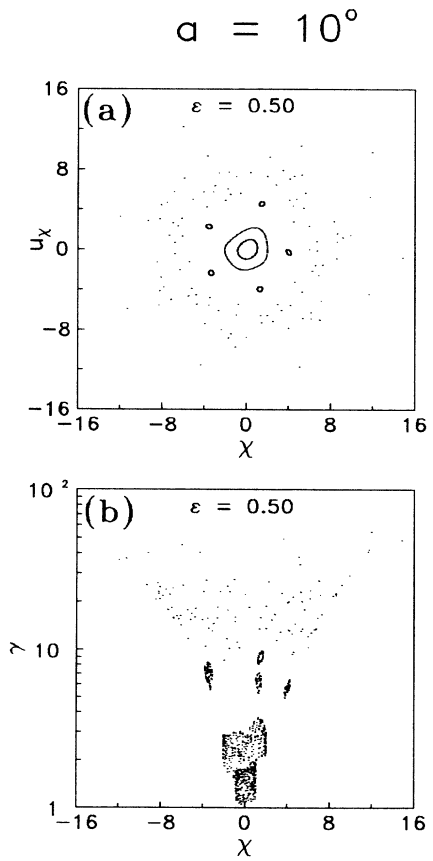

FIG. 7. Relativistic case: (a) Poincaré surfaces of section and (b) total energy, γ, vs normalized position, χ, for propagation angle $a=10°$ and for normalized amplitude $\epsilon=0.50$.

namely, the area bounded by the limiting curve. This area is calculated numerically. By numerical means, though tedious, the area of the domain where the motion is regular can also be estimated. This has been done in our case by carefully scanning χ values (and/or u_x values) in the domain inside the limiting curve, from the center ($\chi=u_x=0$) and moving outwards, until the first set of initial conditions that lead to stochastic behavior is encountered. The ratio of the area of the domain of initial conditions that correspond to regular motion, $A_{\rm reg}$, to the total area of the domain where section points exist, $A_{\rm tot}$, gives also a quantitative measure for the shrinking rate of the regular region as the coupling parameter increases [14]. It is obvious that the ratio $A_{\rm reg}/A_{\rm tot}$ cannot be used in the relativistic case since $A_{\rm tot}$ is infinite. A value similar to this $A_{\rm reg}/A_{\rm tot}$ indicator can be obtained by considering the set of the initial conditions in χ for which invariant tori exist as ϵ varies [15,16]. The semiwidth, $\Delta\chi/2$, of the domain of regular motion has been used in the present work. In the nonrelativistic case, qualitatively speaking, the change of the stochastic region as given by $\Delta\chi/2$ is very similar to that given by the ratio $A_{\rm reg}/A_{\rm tot}$ [16]. The results are presented in Figs. 14(a) and 14(b) for values of the angle of propagation $a=10°$ and 20°, respectively (the triangles correspond to numerical data). It is evident that at $a=10°$ the value of $A_{\rm reg}$ decreases as ϵ increases. The rate of decrease is somewhat slower if one compares it with the $a=20°$ case. We remark that the development of stochasticity for $a=20°$ is as clear by using $\Delta\chi/2$ as it is by using $A_{\rm reg}/A_{\rm tot}$. In the latter case the whole process appears to have three phases: The first appears, in the range of $\epsilon\simeq 0.0-0.03$, where the system behaves as integrable. Near the value $\epsilon\simeq 0.03$ there is an abrupt transition to stochasticity. Then, for $\epsilon\simeq 0.03-0.3$ the stochasticity increases almost linearly. Finally, for higher values of ϵ, an asymptotic (slower development) phase occurs. For higher values of the angle of propagation a, it is almost impossible to make these estimations since the second phase dominates and $A_{\rm reg}$ decreases very rapidly for very low values of ϵ. For instance, for $a=40°$ and $\epsilon\geq 0.05$, it appears that Fig. 3 is the last figure one can get with a numerically measurable $A_{\rm reg}$. The onset of stochasticity seems to coincide with the second phase.

In contrasting the development of stochasticity in the relativistic case versus the nonrelativistic one, we only utilize the semiwidth $\Delta\chi/2$ in Fig. 15 where two cases ($a=10°$, 20°) are shown. There is a feature in this figure that is worth analyzing: For values of ϵ close to zero, $\Delta\chi/2$ goes to infinity as expected from the unbounded character of motion (for every value of ϵ). In the relativistic case the development of stochasticity appears having two phases: The abrupt one for very small values of ϵ up to the values $\epsilon\cong 0.1$ and 0.07 for 10° and 20°, respectively, and a slower one thereafter. For larger values of the propagation angle, the rate of transition gets higher, especially in the first, abrupt, phase. The absence, in the relativistic case, of a phase where the system appears as

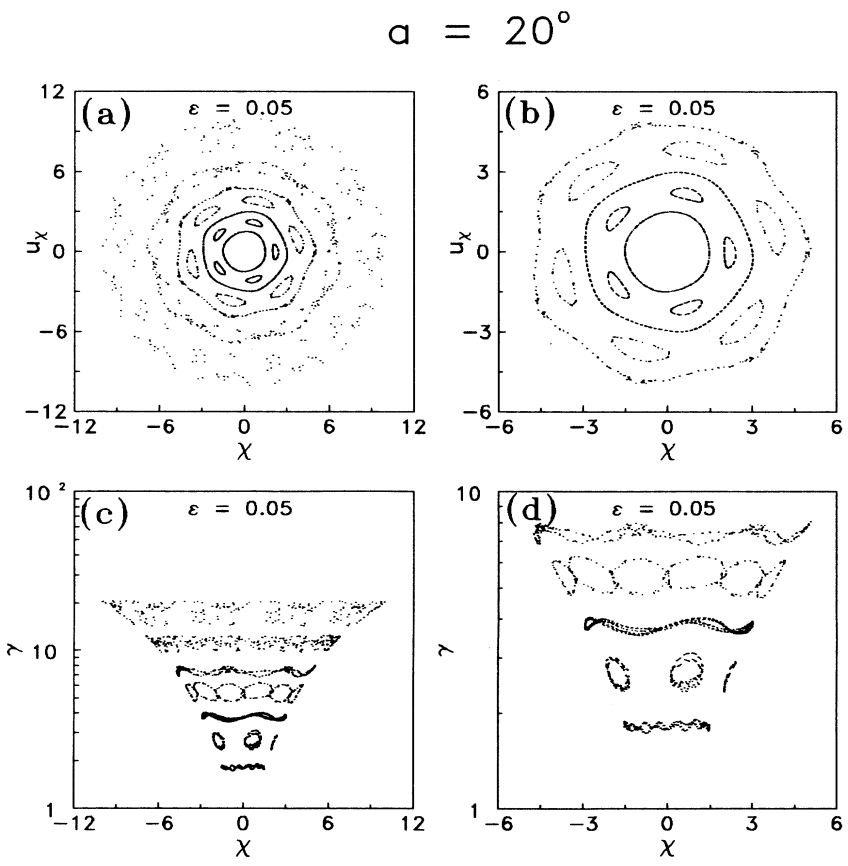

FIG. 8. Relativistic case: Poincaré surfaces of section [(a) and (b)] and total energy, γ, vs normalized position, χ, diagrams [(c) and (d)] for propagation angle $a=20°$ and for normalized amplitude $\epsilon=0.05$. (b) and (d) are fine detail of (a) and (c), respectively.

integrable is due to the unbounded character of motion. The transition rates, on the other hand, between the second phase in the nonrelativistic case and the first phase in the relativistic one, are almost one order of magnitude different.

IV. ENERGY CONSIDERATIONS

In this section we investigate the energies acquired by the accelerated electrons every time their orbits cross the PSS plane. For the relativistic case the energy above the rest-mass energy (in $m_e c^2$ units) is $\gamma - 1$. The respective energy in the nonrelativistic case, to contrast with the relativistic one, is the kinetic energy (expressed, for comparison reasons, in the same $m_e c^2$ units). The energy is plotted as a function of the normalized canonical variable χ. The study is carried out for various values of the angle of propagation and the normalized amplitude. Several initial conditions are simultaneously presented and PSS diagrams are used in parallel for the qualitative assessment of the type of motion in the relativistic case.

A. The relativistic case

The energy is equal to γ [Eq. (3)]. In Fig. 4 many initial conditions are involved. The second column is just a closer look of a subset of the orbits considered. For the angle of propagation $a = 10°$ and amplitude $\epsilon = 0.05$, the motion is, relatively speaking, well organized, i.e., the periodic orbits as well as the quasiperiodic ones have their energies, at the time of PSS plane crossing, varying in narrow bands of ascending level with increasing initial values of χ. Furthermore, these bands do not overlap for well-spaced regular orbits. For the current parameter values this spacing is, relatively speaking, quite narrow.

The groups of Figs. 5–7 refer to the same value of the propagation angle and to different values for the normalized amplitude ϵ, i.e., $\epsilon = 0.20$–0.50. In Fig. 5 the stochastic motion starts developing for orbits with initial values for $|\chi|$ beyond 10. The characteristic bands are clearly shown in Fig. 5(d). However, the band structure disappears completely for orbits originating from the stochastic region. If colors would have been used in Fig. 5(c), it could have been possible for someone to see the whole region $\gamma = 10$–100 being visited by almost everyone of these orbits.

Comparing the results shown in Figs. 5 and 6 leads to the conclusion that, as the normalized amplitude increases, the band structure is not only being destroyed, but also the bandwidth broadens in regions where the motion was periodic or quasiperiodic [Figs. 5(d) and 6(d)]. Therefore, the quasiperiodic orbits acquire energies

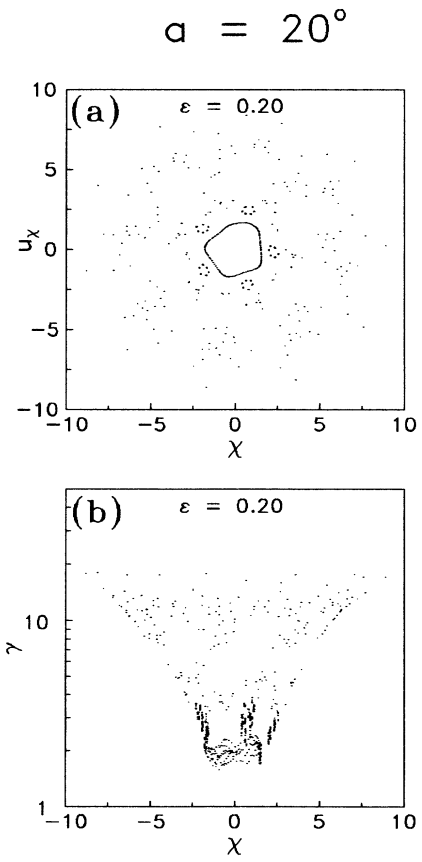

FIG. 9. Relativistic case: (a) Poincaré surfaces of section and (b) total energy, γ, vs normalized position, χ, for propagation angle $a = 20°$ and for normalized amplitude $\epsilon = 0.20$.

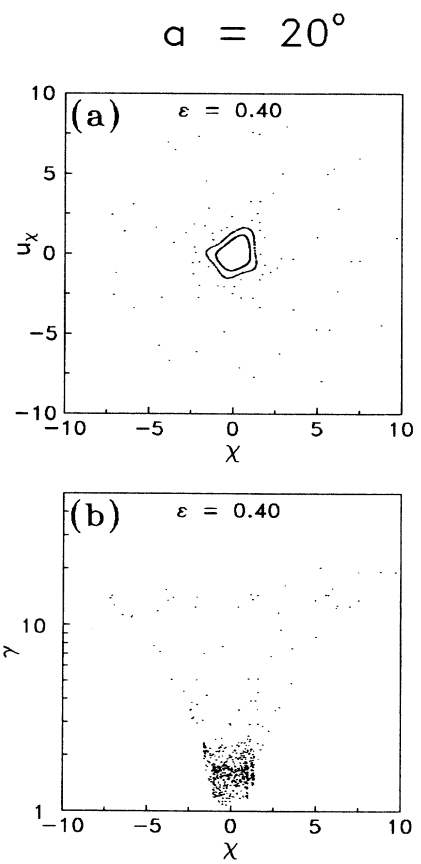

FIG. 10. Relativistic case: (a) Poincaré surfaces of section and (b) total energy, γ, vs normalized position, χ, for propagation angle $a = 20°$ and for normalized amplitude $\epsilon = 0.40$.

in a broader set of values as they cross the PSS plane. As far as the stochastic orbits are concerned, this set of energy values is one or more orders of magnitude broader. In Fig. 6(d) only one stochastic orbit is shown. It is clear from this figure that this dramatic broadening of the energy spectrum at the section points is quite conclusive.

In Figs. 8–11 various orbits are shown for $a=20°$ and $\epsilon=0.05-0.50$. It is expected that the onset of stochasticity will occur at lower values of the amplitude. Indeed, this is supported by the fact that the energy band structure for regular motion is now quite broader for $a=20°$ than the one observed for $a=10°$ [Figs. 4(d) and 8(c)]. In general, when stochastic motion enters into play, it will be more enhanced for higher values of the propagation angle, for the same value of the amplitude, as it is evident from Figs. 5(d) and 9(b). The band structure almost disappears at the value $\epsilon=0.40$ [Fig. 10(b)].

For values of the angle $a=40°$ and beyond, the band structure is conserved only for small values of the amplitude and for orbits of very low initial energy. This initial value of energy decreases rapidly as the angle of propagation increases as seen in Figs. 12 and 13.

From the energy study several important conclusions, concerning the relativistic model, might be drawn: The energy band structure characterizes the regular motion; the energies acquired by the accelerated electrons stay within a relatively narrow band. This is true for the energies at the time of the PSS plane crossing, but also for the energy, at any other time; the latter has been deduced from data of the numerical integration of electron motion. However, these characteristic energy bands are widened as the angle of propagation increases. This broadening also occurs for electrons of higher initial energies. Therefore, a narrow band structure is indicative of small amplitudes and small angles of propagation. If the angle of propagation is appreciable, a narrow band structure characterizes low initial energies. The band structure completely disappears as the amplitude increases. The threshold amplitude value for band destruction decreases as the angle of propagation increases.

In conclusion, in the relativistic model, information concerning the energy is particularly useful for qualitatively characterizing the motion of the accelerated electrons (regular versus chaotic). This information also provides us with a semiquantitative assessment of the threshold for stochastic motion either in the normalized amplitude, ϵ, or the angle of propagation with respect to the electron beam, a. Since the energy can be directly measured, the energy diagrams provide a very useful tool for studying the accelerating electron dynamics a step closer

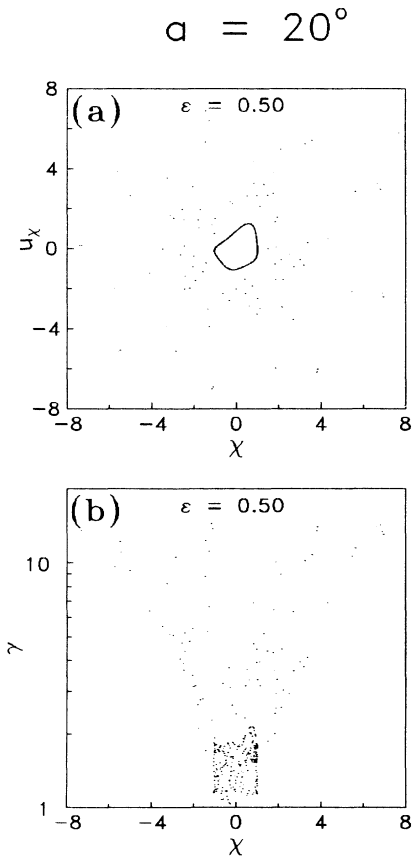

FIG. 11. Relativistic case: (a) Poincaré surfaces of section and (b) total energy, γ, vs normalized position, χ, for propagation angle $a=20°$ and for normalized amplitude $\epsilon=0.50$.

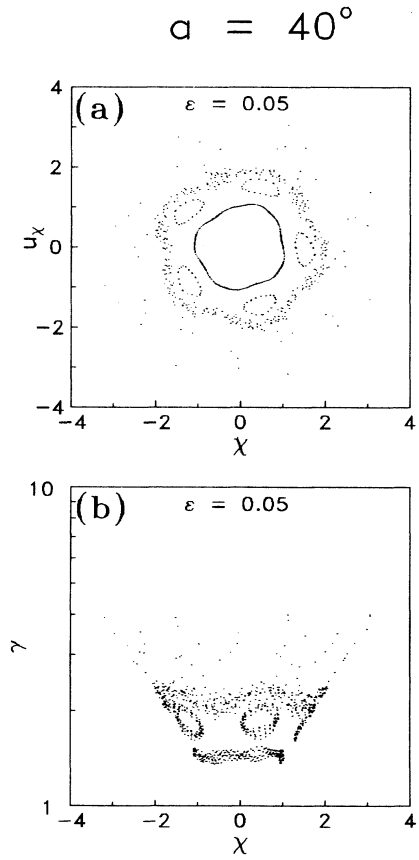

FIG. 12. Relativistic case: (a) Poincaré surfaces of section and (b) total energy, γ, vs normalized position, χ, for propagation angle $a=40°$ and for normalized amplitude $\epsilon=0.05$.

towards the experimental reality. They might be alternatively used in the place of Poincaré surfaces of section.

B. The nonrelativistic case

Low kinetic energies are distributed in the nonrelativistic case in, approximately, the same was as the relativistic ones for values of the respective γ's close to 1. As the kinetic energy increases, the approximation ceases to be valid and enormous deviations in the distribution appear as expected: All the energy levels are distributed in χ, roughly, between -2 and 2 and the bounded character of motion restricts the energy at, relatively speaking, very low values. In Fig. 16 two cases for angles of propagation $a=10°$ and 20° are presented for two indicative values of the normalized amplitude $\epsilon=0.05$ and 0.20. The most dense part of the distribution appears at kinetic energies where the nonrelativistic approximation is a valid description of the physical system at hand.

V. STABILITY AND THE DIAGRAMS OF CHARACTERISTICS

A. General methodology

The algorithm to find a periodic orbit is based on the well-known Newton-Raphson procedure. Once a periodic orbit is found, the corresponding monodromy matrix $\mathbf{M}(T)$ is calculated by integrating the variational equations over one period T of the periodic orbit. The solutions of the variational equations are of the form

$$\Delta\mathbf{X}=\mathbf{M}(T)\cdot\Delta\mathbf{X}_0 , \tag{15}$$

where $\mathbf{X}$ is the column vector of the coordinates (χ,ξ) and their conjugate momenta (u_x,u_ξ) and $\Delta\mathbf{X}_0$ the displacement from the periodic orbit at time $t=0$. Since the system under consideration is conservative (Hamiltonian) one has

$$\det\mathbf{M}(T)=1 . \tag{16}$$

The stability of a periodic orbit is determined by the eigenvalues λ of the monodromy matrix $\mathbf{M}(T)$. For conservative dynamical systems two eigenvalues are equal to 1. The remaining two are λ and $1/\lambda$. These eigenvalues

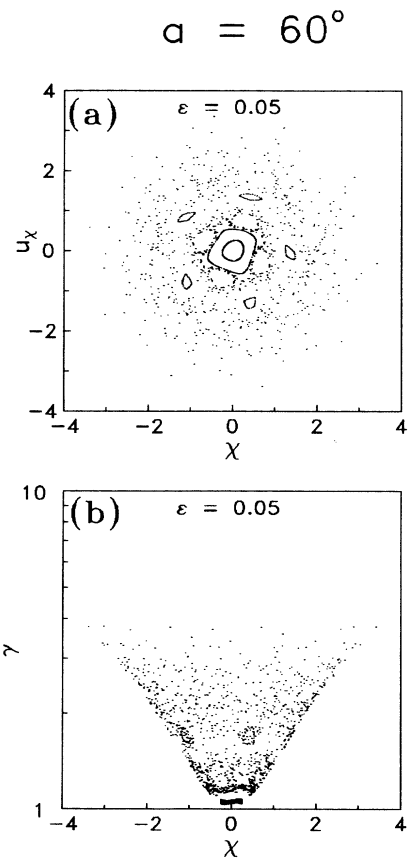

FIG. 13. Relativistic case: (a) Poincaré surfaces of section and (b) total energy, γ, vs normalized position, χ, for propagation angle $a=60°$ and for normalized amplitude $\epsilon=0.05$.

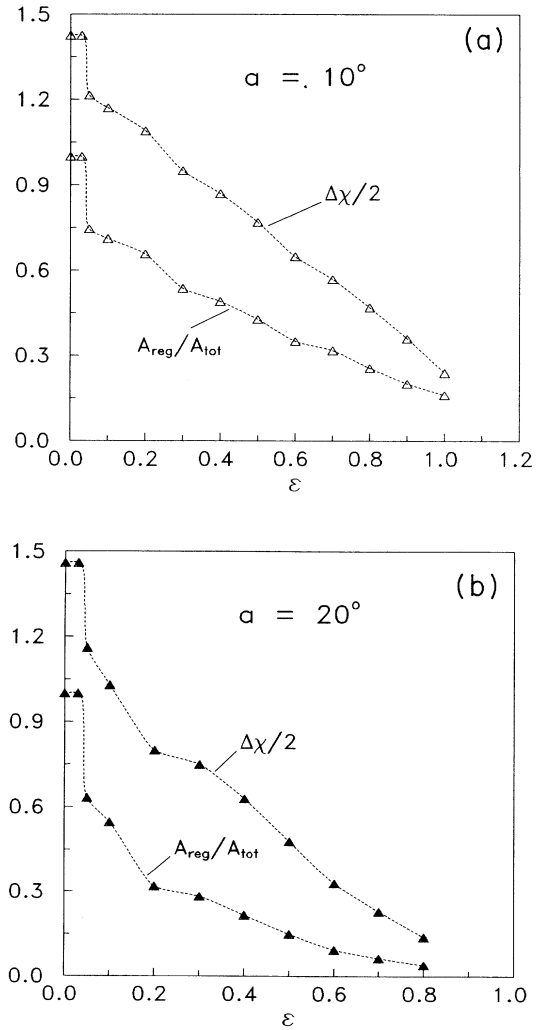

FIG. 14. Nonrelativistic case: The semiwidth of the region where the motion is regular, $\Delta\chi/2$, and the ratio of the area of that region to the total area of the Poincaré surfaces of section, A_{reg}/A_{tot}, vs the normalized amplitude, ϵ. The angle of propagation is (a) $a=10°$, (b) $a=20°$, and at $\epsilon=0$, $A_{reg}/A_{tot}=1$.

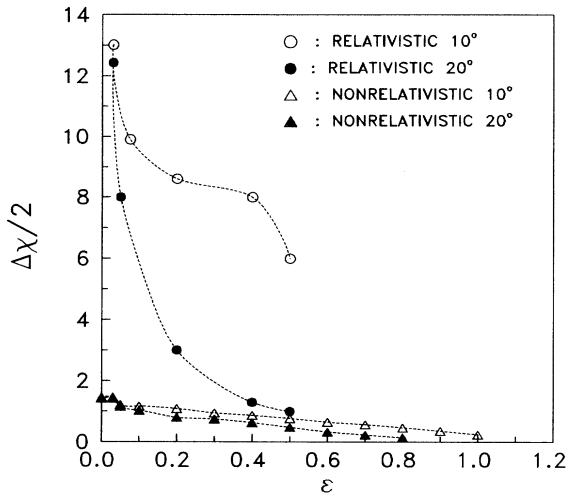

FIG. 15. The semiwidth of the region where the motion is regular, $\Delta\chi/2$, for the relativistic (circles) and the nonrelativistic case (triangles) vs the normalized amplitude, ϵ, and for propagation angle $a=10°$ and 20°.

can be written in exponential form as follows:

$$\lambda=e^{sT},\quad \frac{1}{\lambda}=e^{-sT}, \tag{17}$$

where s is the characteristic exponent. For a stable periodic orbit s is purely imaginary, $s=\pm i\omega$, while for an unstable periodic orbit s is real, $s=\pm\omega$. In the stable case, ω is the frequency with which a trajectory neighboring a periodic orbit rotates around it. In this work the stability of a periodic orbit is expressed through the stability index α [17],

$$\alpha=\frac{1}{2}\left[\lambda+\frac{1}{\lambda}\right]=\frac{e^{sT}+e^{-sT}}{2}. \tag{18}$$

If $|\alpha|<1$ (i.e., $s=\pm i\omega$) the periodic orbit is stable, while if $|\alpha|>1$ (i.e., $s=\pm\omega$), it is unstable.

The dynamical behavior of the system under consideration is investigated by determining the periodic orbits and their stability by continuously varying the coupling parameter ϵ. Following the continuous evolution of a family of periodic orbits one finds its bifurcations if they exist. The plots of the initial conditions of periodic orbits with respect to the coupling parameter ϵ are the well-known diagrams of characteristics. New families bifurcate from the original family whenever the periodic orbit is stable with stability parameter $\alpha=\cos(\omega T)=\cos(2\pi m/n)$, where m,n are integers. Then the period of the new family is nT. The ratio m/n is the so-called rotation number.

B. Investigation

The Poincaré surfaces of section have been used as a diagnostic tool for the degree of development of the stochastic motion. However, they can also be used, in conjunction with the stability diagrams and the diagrams of

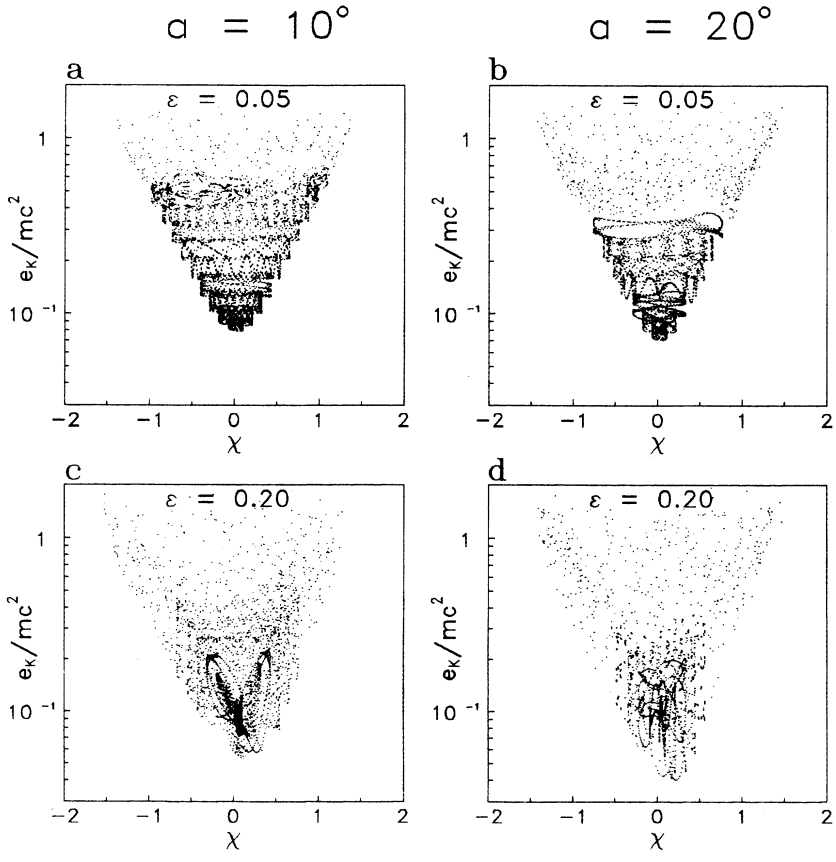

FIG. 16. Nonrelativistic case: Normalized kinetic energy, e_K/mc^2, vs normalized position, χ, diagrams for propagation angles $a=10°$, 20° and for normalized amplitudes $\epsilon=0.05$ [(a), (b)] and 0.20 [(c), (d)].

characteristics, for the study of the evolution of a family of periodic orbits by changing the coupling parameter ϵ.

The characterization *main family* (MF) will refer in the following to a family of periodic orbits whose representation on a surface of section is a single point, the so-called invariant point (χ_0, u_{x0}). In order to find the principal periodic orbit of the MF one utilizes the normalized unperturbed Hamiltonian functions

$$h_{\mathrm{NR}}=\frac{1}{2}(u_x^2+u_\xi^2)+\frac{1}{2}\chi^2-\frac{u_\xi}{n_z} \tag{19}$$

and

$$h_{\mathrm{R}}=(u_x^2+u_\xi^2+\chi^2+1)^{1/2}-\frac{u_\xi}{n_z}\ . \tag{20}$$

It is evident, from the form of these Hamiltonians, that the principal periodic orbit in both cases is the one with $u_{x0}=\chi_0=0$, i.e., the origin of the axes on a (χ, u_x) surface of section. Therefore, the diagrams of characteristics are curves originating at $\chi_0=0$, for $\epsilon=0$.

Let us now "perturb" the system ($\epsilon\neq 0$) and follow the evolution of the MF for several angles. In Figs. 17 and 18 the stability diagrams are given for the relativistic and nonrelativistic cases, respectively. From Fig. 19, on the other hand, it is evident that, irrespectively of the angle of propagation, the principal periodic orbit at $\epsilon=0.0$ is stable since the stability index α is confined in the region from -0.5 to 0.5 both in the relativistic and the nonrelativistic cases. It is also observed (Fig. 18) that, in the nonrelativistic case, the stability curves reach a minimum below the value $\alpha=-1$ (unstable) for propagation angles $a\geq 10°$. Furthermore, this minimum drops as the angle, a, increases. The presence of this minimum allows the correspondence of two different values of the normalized amplitude ϵ to the same value of the stability index α. Especially in the stability region in Fig. 18 ($\alpha>-1$) "bubble" formation is allowed [18,19]; we will pursue this issue extensively in the next section. Beyond $a=50°$ the periodic orbits become very unstable ($\alpha\ll -1$) for ϵ larger than 0.5 in the nonrelativistic case.

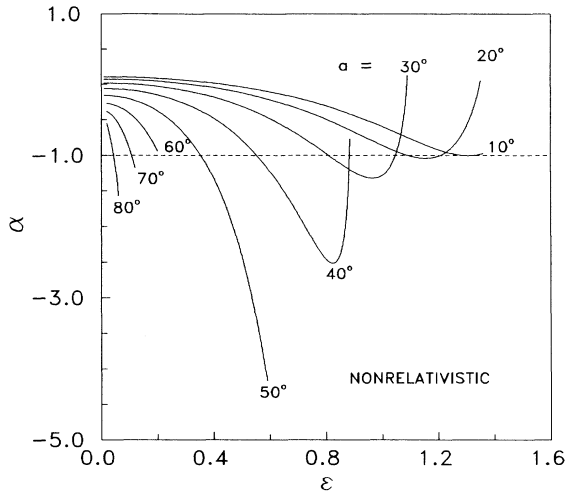

FIG. 18. Nonrelativistic case: Stability diagrams (stability index, α, vs normalized amplitude, ϵ) for several values of the propagation angle, a. The dashed horizontal line separates the stable region (upper) from the unstable one (lower).

A difference also appears in the characteristic diagrams (Figs. 20 and 21). At a given value of the normalized amplitude ϵ, the value of the initial spatial position χ for periodic orbits decreases as the angle of the propagation angle a increases for the nonrelativistic case (Fig. 20), while the opposite occurs for the relativistic one [as far as the initial absolute value of χ is concerned (Fig. 21)]. Furthermore, for large values of the propagation angle, the characteristic curves are confined in the small ϵ region in the nonrelativistic case, while, in the relativistic one, they cover a wide domain, irrespectively of the propagation angle.

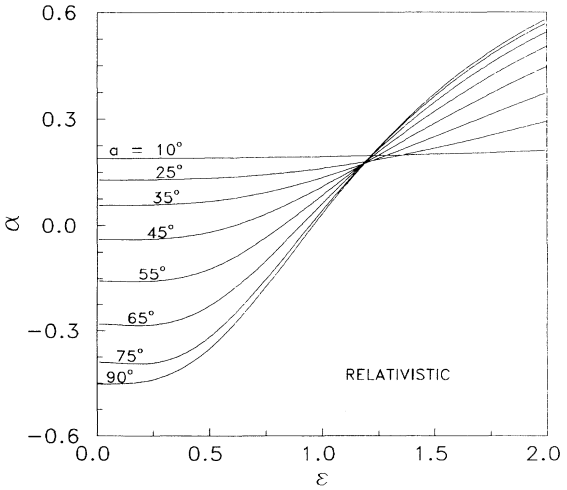

FIG. 17. Relativistic case: Stability diagrams (stability index, α, vs normalized amplitude, ϵ) for several values of the propagation angle, a.

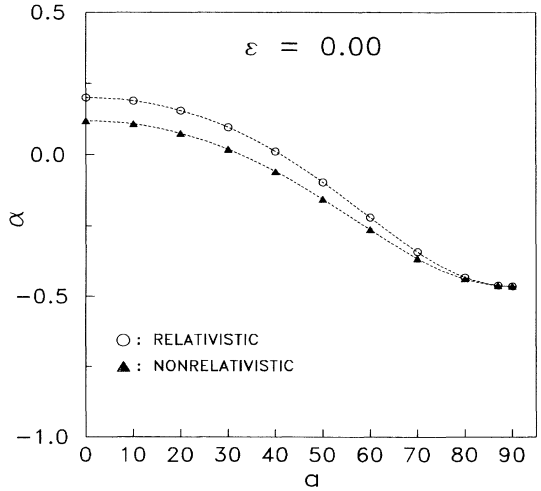

FIG. 19. Stability index, α, vs angle of propagation, a, in the unperturbed case (normalized amplitude $\epsilon=0.00$) for the relativistic (circles) and nonrelativistic (solid triangles) models.

As ϵ becomes finite, a strong qualitative difference appears between the relativistic and nonrelativistic cases (Figs. 17 and 18). In the relativistic case the value of α increases with ϵ, but the MF never turns unstable, at least for $\epsilon \leq 2$ (Fig. 17). In the nonrelativistic case, the value of α decreases with ϵ (for small ϵ) and there is always a critical value of ϵ (Fig. 18) at which the MF turns unstable ($\alpha < -1$). For larger ϵ, it seems that α increases again after reaching a minimum value and becomes of the stable type ($-1 < \alpha < 1$) again, while for still larger ϵ it seems that α becomes again unstable ($\alpha > 1$).

Another way to explore the difference between the relativistic and the nonrelativistic cases is by investigating the bifurcations that can be generated in these two cases for the same finite value of the coupling parameter ϵ. The question is to find the possible irreducible ratio of integers m/n which can be related to the respective stability index through the equation $\alpha = \cos(2\pi m/n)$. Since the number of the bifurcations (and, so, the number of the families being generated) is immense, we adopt the following procedure: First, we fix the value of the normalized amplitude to $\epsilon = 0.01$ (it does not matter what its value is as long as $\epsilon \neq 0$) and subsequently the stability indices are calculated for various values of the angle of propagation a. For each calculated value of the stability index we find the irreducible ratio m/n with $n \leq N_0$ with N_0 equal, say, to 100 [denoted by $(m/n)_0$] which minimizes the value of $|\arccos(\alpha) - 2\pi(m/n)_0|$. These ratios are the labels at the calculated points in Fig. 22. For example, for $a = 20°$ and nonrelativistic treatment $\alpha = 0.074\,448$, $\arccos(\alpha) \cong 85.730\,49°$ while $360 \times \frac{21}{88} \cong 85.909\,09$ and the difference between those two angles is the smallest possible (for $n \leq 100$). If one takes the values of the stability index α at $a = 10°$ as reference values the diagram of ΔN vs a can be constructed (Fig. 23). ΔN denotes the number of irreducible ratios (m/n), with n being equal or smaller than a chosen integer N_0 ($n \leq N_0$), which lie between the respective ratios for $a = 10°$ and the current value of a. For example, for the relativistic case, we have from Fig. 22 that $(m/n)_0 = \frac{20}{91}$ and $\frac{18}{59}$ for $a = 10°$ and 70°, respectively; ΔN in this case is the number of irreducible ratios, m/n, with $n \leq N_0$ that satisfy the inequality $\frac{20}{91} < m/n \leq \frac{18}{59}$ (for $N_0 = 100$, $\Delta N = 259$). In Fig. 23 ΔN is normalized to N_0^2 with $N_0 = 100$. However, the curves for $N_0 = 200$, 300, etc. are extremely close to those for $N_0 = 100$.

It is clear from Fig. 23 that the number of bifurcations m/n with $n \leq N_0$ increases dramatically at $a \simeq 87.5°$ for the nonrelativistic case while it saturates for the relativistic one. This dramatic effect, which depicts the fundamental difference concerning the density of the bifurcating families in these two cases, becomes more pronounced as the coupling parameter, ϵ, increases. In Fig. 24, the critical value of ϵ where ΔN starts diverging, ϵ_{crit},

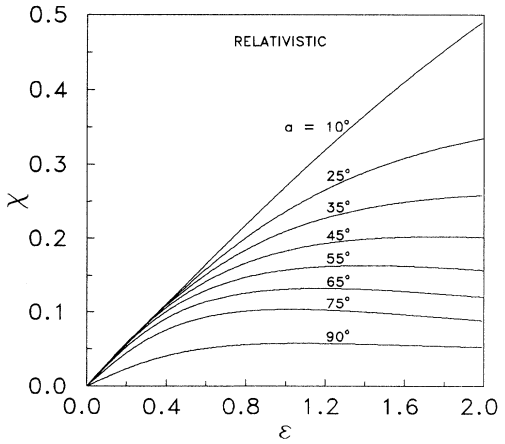

FIG. 20. Relativistic case: Diagrams of characteristics (spatial initial conditions, χ, of periodic orbits vs normalized amplitude ϵ), for several values of the propagation angle a.

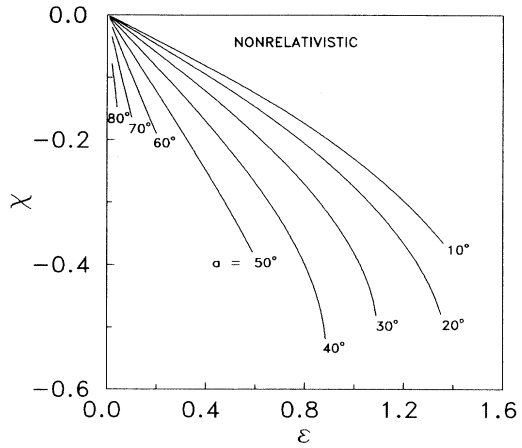

FIG. 21. Nonrelativistic case: Diagrams of characteristics (spatial initial conditions, χ, of periodic orbits vs normalized amplitude ϵ), for several values of the propagation angle a.

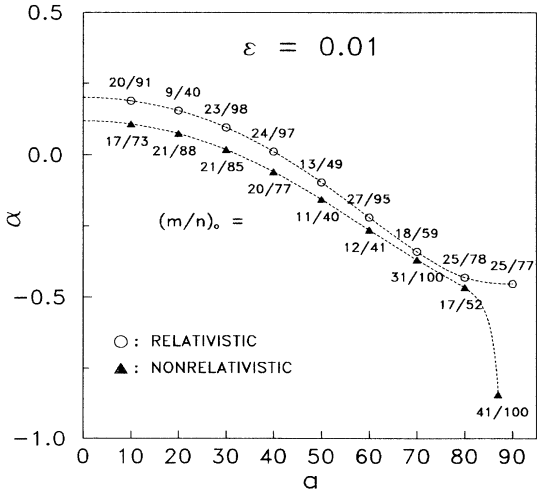

FIG. 22. Stability index, α, vs angle of propagation a, in the perturbed case, $\epsilon = 0.01$, for the relativistic (circles) and nonrelativistic (solid triangles) models. For each calculated value of the stability index the irreducible ratio m/n with $n \leq 100$ [denoted by $(m/n)_0$] that minimizes the value of $|\arccos(\alpha) - 2\pi(m/n)_0]$ labels the data points.

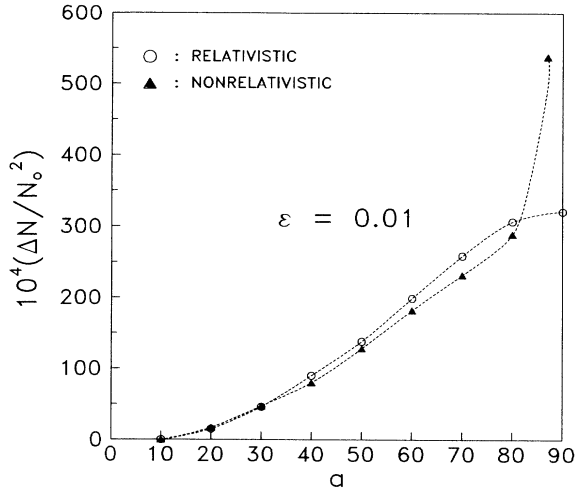

FIG. 23. Diagram of ΔN [normalized to $(N_0/100)^2$] vs propagation angle a. ΔN denotes the number of irreducible ratios (m/n), with $n \leq N_0$, which lie between the respective irreducible ratios of Fig. 22 for $a=10°$ (taken as reference) and for the chosen value of a.

is given as a function of the propagation angle a, for few calculated cases. This diagram solely characterizes the nonrelativistic case. In Fig. 25, on the other hand, the PSS diagrams for two combinations of propagation angle and amplitude, in the neighborhood of ϵ_{crit}, are contrasted against their respective ones at slightly lower values of ϵ (with the same initial conditions). The results in Fig. 24 seem to be in accordance with the qualitative assessment one can make by observing the destruction of the "inner" islands, Fig. 25, as ϵ approaches the critical value. However, the intriguing feature of the "pockets" of regular motion near the limiting curve appears in one of the cases.

In conclusion, it has been observed in the relativistic

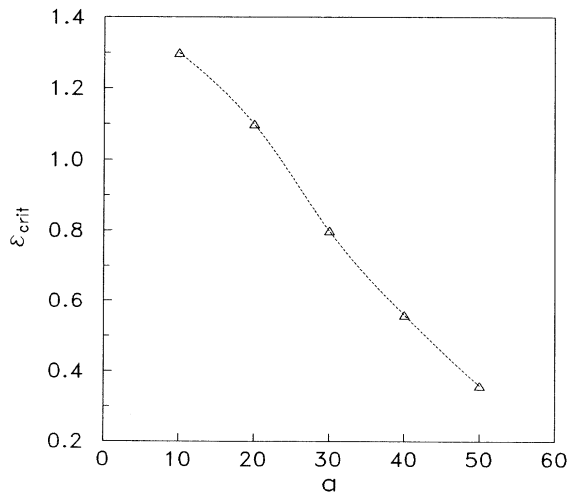

FIG. 24. Nonrelativistic case: The value of the normalized amplitude where ΔN of Fig. 23 starts diverging, ϵ_{crit}, vs the propagation angle a, for several calculated cases (triangles).

case that the main periodic orbit never turns unstable and, therefore, there is always a region of stability. In contrast, in the nonrelativistic case, large-scale stochasticity is observed when the amplitude increases, which is accompanied with a dramatic proliferation of bifurcations of the MF. Therefore, period-doubling bifurcations of the MF seem to be the dominant mechanism for the onset of stochasticity in the nonrelativistic case. However, this mechanism seems to be absent in the relativistic model at least for values of the normalized amplitude, ϵ, below 2. However, in the relativistic case a period-doubling sequence may be produced from the "daughter" families generated, through bifurcation, from the MF.

VI. BIFURCATION SEQUENCE

In this section we investigate the bifurcation sequence in the diagrams of characteristics of the nonrelativistic case. Without compromising the generality of the conclusions to be drawn, we arbitrarily choose the value of the angle of propagation to be 30°, and study the bifurcations in the diagram of characteristics. It is also being kept track of the stability index on separate stability diagrams.

Starting with the MF on Fig. 26(a) we observe that for values of the normalized amplitude ϵ between 0.0 and $\simeq 0.81$ this family is stable (solid line segment 0-1). At $\epsilon \simeq 0.81$, a period-doubling bifurcation $(\alpha=-1)$ takes place. This family is unstable between $\epsilon \simeq 0.81$ and $\epsilon \simeq 1.04$ but the instability is "mild" (i.e., α is not much smaller than -1, $\alpha_{min} \simeq -1.3184$ at $\epsilon \simeq 0.97$). The region that follows (solid line segment 5-11) is stable. The end point (11) at $\epsilon \simeq 1.0953$ $(\alpha=+1)$ is an inflection point in the diagram of characteristics. Beyond this value of ϵ, the main family does not exist. If we reduce the normalized amplitude, we find another branch of the main family which is "strongly unstable" ($\alpha_{max} \simeq 227$ at $\epsilon \simeq 0.369$). At the end point of the latter (12) the stability parameter returns to the value $+1$ at $\epsilon=0.0$ [Fig. 26(b)]. It is evident that the MF strongly depends on the initial conditions: For small initial values of the normalized position χ, χ_0, the orbits are stable for a relatively wide spectrum of values of ϵ; while if χ_0 is relatively large, the orbits become extremely unstable.

We turn now to the branch which bifurcates, in a period-doubling fashion, from point 1 in Fig. 26(a). It is well known [18,19] that when the stability index α reaches the value -1, the MF generates by bifurcation two stable branches of a double period family, which has a starting value of α equal to $+1$. In our case, the bifurcating family is *inverse* (i.e., the family exists for smaller ϵ, that is, for values for ϵ for which the MF is stable). Then, according to Poincaré, the bifurcating family is initially *unstable.* On the other hand, at point 5 there is a direct bifurcation of a period-doubling family, i.e., in the direction in which the MF is unstable. Thus, the bifurcating family is initially stable [branches 5-4 and 5-4′ in Fig. 26(a)] according to Poincaré. Furthermore, these families are *nonsymmetric:* The unstable family (bifurcating from point 1) corresponds to positive values of the normalized canonical momentum u_x, while the stable one

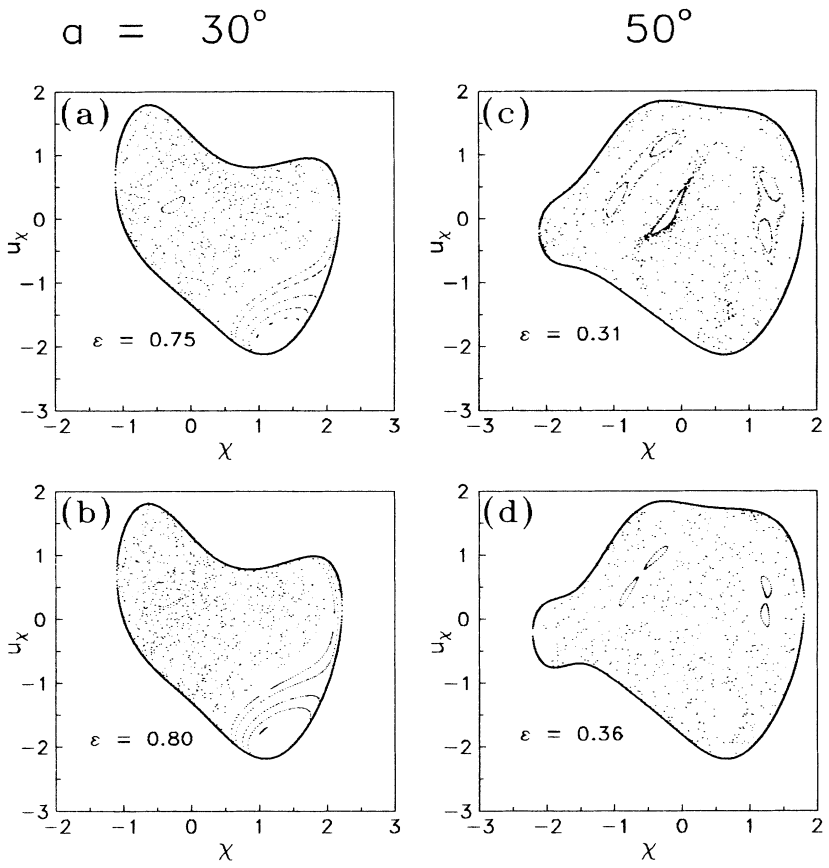

FIG. 25. Nonrelativistic case: Poincaré surfaces of section referring to two cases appearing in Fig. 23: (a) $a=30°$, $\epsilon=0.75$; (b) $a=30°$, $\epsilon=0.80$; (c) $a=50°$, $\epsilon=0.31$; (d) $a=50°$, $\epsilon=0.36$.

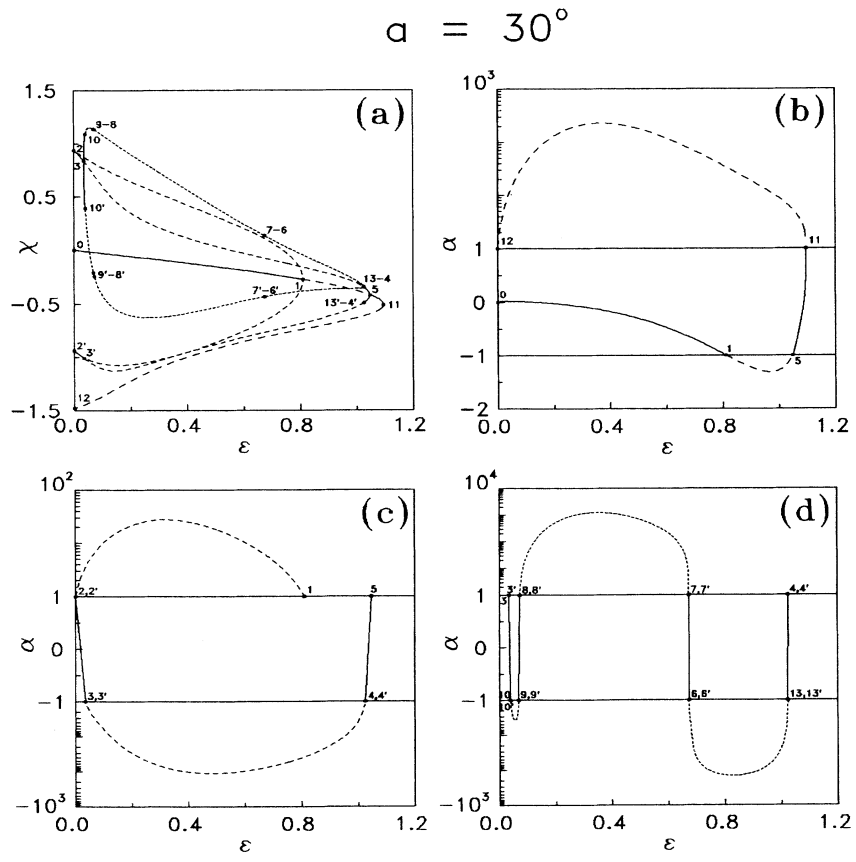

FIG. 26. Nonrelativistic case: (a) Diagrams of characteristics for the following: (i) The main family 0-1-5-11-12 with its respective stability diagram (b). (ii) The inversely bifurcating at the points (1) and (5) "daughter" branches 1-2-3-4-5 and 1-2′-3′-4′-5 (forming an "inverse bubble") with their respective stability diagram (c). (iii) The bifurcating at the points (3) and (4) "granddaughter" branches 3-10-9-8-7-6-13-4 and 3-10′-9′-8′-7′-6′-13′-4 [analogous branches bifurcate at (3′) and (4′)] with their respective stability diagram (d). The angle of propagation is $a=30°$.

(bifurcating from 5 has negative u_x's. Therefore, a new feature appears in this "*inverse bubble*": In the parameter space (ϵ,χ,u_x), the bubble is *nonplanar*. The sign of the momentum switches at points 2 and 2′ at $\epsilon=0$.

As far as the stability diagram of the aforementioned bubble is concerned, strongly unstable orbits exist for values of ϵ between 0.0 and 0.81. Specifically, in the segment 1-2 (and 1-2′), the stability index α reaches it maximum value, $\alpha_{\max}\simeq 27.7$, at $\epsilon\simeq 0.3175$ [Figs. 26(a) and 26(c)]. At zero amplitude, the stability index returns to the value $+1$ (points 2 and 2′). In a very narrow region between $\epsilon=0.0$ and $\epsilon\simeq 0.0381$ the bifurcating family from point 5 is stable (solid line segments 2-3 and 2′-3′). At the end point of this region (3 and 3′) a new period-doubling bifurcation occurs ($\alpha=-1$) which generates new family with a period 4 times the period of the MF. This family is stable close to 3 (and 3′), then continues as unstable, and again becomes stable close to 5, joining the double period family from 5 at the point 4 (and also 4′). The second stable region extends from $\epsilon\simeq 1.023$ to $\epsilon\simeq 1.047$ and its origin (points 4 and 4′) coincides with $\alpha=-1$. Therefore, a period-doubling bifurcation is expected there. The period four family exhibits very high (negative) values of the stability index α: at $\epsilon\simeq 0.485$ one has $\alpha_{\min}\simeq -111.8$. The fact to be pointed out is the existence of highly unstable orbits for very small values of the normalized amplitude, ϵ, for moderate initial values of χ, both in the MF and in its bifurcating families.

We finally turn to the families generated by the period-doubling bifurcation at points 3 and 3′ of the bubble 1-2(2′)-3(3′)-4(4′)-5 [Figs. 26(a) and 26(d)]. Due to the existence of a second period-doubling bifurcation point on this bubble (points 4 and 4′), the families of period four (with respect to the MF) also form a bubble. This bubble consists of a direct (from point 3) and an inverse (from point 4) bifurcating family. It is a planar bubble [although out of the (χ,ϵ) plane]. Therefore, the succession of stable and unstable regions are expected to occur on the two branches at the same values of the normalized amplitude, ϵ. As it is shown in Fig. 26(a) this is indeed the case. For the sake of clarity, only the forward bubble between the points 3 and 4 is shown (a second forward one exists between points 3′ and 4′). The bifurcating families from points 3 and 4 are stable as expected for a typical forward bubble; however, it spans an extremely narrow region in ϵ, i.e., from $\epsilon\simeq 0.038\,06$ (at the points 3 and 3′) to $\epsilon\simeq 0.039\,97$ (at the points 10 and 10′) and from $\epsilon\simeq 1.023$ (at the points 13 and 13′) to $\epsilon\simeq 1.025$ (at the points 4 and 4′). At the end points of these regions [(10,10′) and (13,13′)] period-doubling bifurcations occur. The region that follows points 10 (and 10′), up to $\epsilon\simeq 0.0682$, is unstable with $\alpha_{\min}\simeq -3.8$ at $\epsilon\simeq 0.0548$. A tiny stable region succeeds the unstable one [segment 9(9′)-8(8′)] from $\epsilon\simeq 0.0682$ to $\epsilon\simeq 0.0728$. Thereafter, a wide unstable region follows after a period-conserving bifurcation ($\alpha=+1$) at the end points of the stable region (8 and 8′). This unstable region extends from $\epsilon\simeq 0.0723$ up to $\epsilon\leq 0.67$ and exhibits very high values of the stability index, i.e., $\alpha_{\max}\simeq 1236$ at $\epsilon\simeq 0.349\,37$. It has been found that a minuscule stable region follows for ϵ up to about 0.67 [segment 7(7′)-6(6′)]. A period-doubling bifurcation is naturally expected at point 6 (and 6′) and the region that follows up to point 13 (and 13′) is unstable extending from $\epsilon\simeq 0.67$ up to $\epsilon\simeq 1.023$; the stability index attains its minimum, $\alpha_{\min}\simeq 146$ at $\epsilon\simeq 0.82$. The bubble under consideration closes at point 4 (and 4′) through a narrow stable region [segment 13(13′)-4(4′)] from $\epsilon\simeq 1.023$ (at the points 13 and 13′) to $\epsilon\simeq 1.025$ (at points 4 and 4′). Finally, the bifurcations that occur along the branches of this bubble are expected to lead to the formation of secondary bubbles.

It is worth observing that the extend of the stable regions on the aforementioned forward bubble are extremely narrow, even narrower than the respective regions on the *nonplanar "inverse bubble."* This is evident by contrasting Figs. 26(c) and 26(d). Extended regions of stability occur only for the MF [Fig. 26(d)]. Another point worth mentioning is the trend towards progressively higher absolute values of the stability index as one moves from parent to daughter bifurcating families. The appearance of "pockets" of regular motion mentioned in Sec. III may be tied upon the possibility of existence of narrow stability regions even for relatively large initial values of the spatial variable as we saw. However, as far as the precise morphology of bubbles of order higher than the one already encountered is concerned, this stays an open issue and, perhaps, a quite tedious task for future investigation.

VII. SUMMARY OF CONCLUSIONS

One essential difference between the nonrelativistic and relativistic cases is the permissible area of motion: In the former case the motion is bounded in a part or parts of the phase space, while, in the latter one, the motion is unbounded since the phase space itself has infinite extent. An important conclusion from this fact is that the well-known Poincaré recurrence theorem, valid in the nonrelativistic case, ceases to be valid in the relativistic one Nevertheless, there still remains an open question about the possibility a specific set of initial conditions to validate this theorem in the relativistic case. However, the scientific literature is currently rather conclusive about the inapplicability of the recurrence theorem in unbounded systems: It recently became known that the transport phenomena, investigated via the so-called lobe dynamics, depend upon the formation of the homoclinic tangles. This formation depends drastically upon the character of motion [20] (bounded versus unbounded).

Furthermore, the nonrelativistic motion is characterized by the possibility of having two or several disjoint areas where the motion is permissible. This feature, a mere outcome of the equations providing the limiting curves, has not been examined in the present work; it is an issue under current investigation. However, upon an appropriate choice of the parameters, our preliminary results show that communication between disjoint regions of permissible motion (through the second spatial canonical variable), on a Poincaré surface of section, is possible.

By contrasting PSS of the relativistic and nonrelativistic cases, it is found that the rate of increase of the stochastic region with the normalized amplitude, which

plays the role of the perturbation (or coupling) parameter, is much more pronounced in the relativistic case. This has been quantitatively confirmed (through the numerical data) by contrasting the time it takes for a stochastic orbit to cross the PSS plane. This time, which fluctuates considerably between successive crossings if the orbit is stochastic, increases, in an average sense, much more rapidly with the perturbation parameter in the relativistic case than it does in the nonrelativistic one. Long crossing times, on the other hand, clearly imply in general crossing points on a PSS plane far from the center $\chi_0=u_{x0}=0$ and, thus, a wider stochastic region. Therefore, the stochastic transition is much faster in the relativistic case. However, due to the unbounded character of motion, the width of the region for regular motion is much wider in the relativistic case than the nonrelativistic one.

The transition rate to stochasticity is found to be characterized by three phases in the nonrelativistic case: A narrow one in which the system appears as integrable, an abrupt transition to stochasticity, and a slower phase for higher values of the perturbation parameter. This conclusion seems to be in accordance with analogous observations in Ref. [5]. In the relativistic case, the development of stochasticity is characterized by two phases: An abrupt one, for very small values of the perturbation parameter, followed by a slower one. This separation of phases is more evident at the propagation angle $a=20°$, while for larger values of a, the rate of the transition gets higher, especially in the first, abrupt, phase. The absence, in the relativistic case, of a phase where the system appears as integrable is merely due to the unbounded character of motion. There is also a considerable difference (of almost one order of magnitude) in the transition rates between the second phase in the nonrelativistic case and the first phase in the relativistic one.

The more intriguing feature of the period-doubling bifurcations in the nonrelativistic case is the nature of the bubble bifurcating from the MF. Instead of (a) a period-doubling bifurcation to two stable branches when the stability index reaches the value -1 (switching to $+1$), (b) the formation of a bubble when the branches close at the second bifurcation point (where the stability index attains the value ± 1 again), the situation in the nonrelativistic case at hand is quite different: The bifurcating family is inverse (i.e., its branches turn backwards), thus initially unstable, and nonsymmetric (i.e., parts of the two branches correspond to opposite values of the respective conjugate momenta, u_x). In the parameter space of the perturbation parameter and the conjugate pair (χ,u_x), the bubble is nonplanar.

The transition rate and the degree of stochasticity has been illustrated through the diagrams of the characteristic curves. We further illustrate the nature of the aforementioned novel bubble as far as the stochastic behavior is concerned as follows.

This bubble, solely characterizing the nonrelativistic case, is certainly a different route to chaos than the typical bubble: In general, the typical bubble is formed as the perturbation parameter, ϵ, increases [18,19]. For small values of ϵ the motion stays regular. As ϵ passes through a certain value, say ϵ_1, a direct period-doubling bifurcation is born. An inverse bifurcation is also born as ϵ passes through a second value $\epsilon_2>\epsilon_1$. The typical bubble is now formed by simply connecting the direct and the inverse bifurcations. At the value ϵ_1 the motion is characterized by a small degree of stochasticity. As ϵ increases beyond ϵ_1, the degree of stochasticity increases reaching its maximum at a value of the perturbation parameter, ϵ, lying between ϵ_1 and ϵ_2. Therefore, for values of ϵ near (but less than) ϵ_2 the motion is characterized by a small degree of stochasticity and regains its regular character for values $\epsilon>\epsilon_2$. On the other hand, the inverse bubble of our case extends backwards, that is, it exists for small values of the perturbation parameter ϵ ($\epsilon\rightarrow 0^+$). Therefore, for small values of ϵ the motion is characterized by a small degree of stochasticity which increases as ϵ increases. The degree of stochasticity is reinforced by the fact that the main family of periodic orbits extends up to maximum value of ϵ (Fig. 26) and then returns *backwards* as *unstable,* i.e., towards small values of $\epsilon(\epsilon\rightarrow 0^+)$. Thus, it is evident that tantamount differences exist between the dynamical behavior of a typical bubble and the inverse one.

This inverse bubble formation is a novel dynamical behavior that characterizes the system at hand in its nonrelativistic approximation. In contrast, the relativistic case is characterized by the fact that the main family *never turns unstable* (at least for values of the perturbation parameter, ϵ, less than 2) *irrespectively* of the angle of propagation, a. Thus, there always exists a region of stability in this case. This novel behavior is tightly related to the behavior of the *main family.* It should be remarked that this family represents the periodic orbits $u_x=\chi=0$, where a nonrelativistic approximation may look appropriate if one naively overlooks the tantamount differences in the dynamical behavior that this family exhibits in these two models.

In the nonrelativistic case there is always a value of the normalized amplitude ϵ for every value of the angle a at which the MF turns unstable. For this reason, a thorough stability study has been made for this case whose conclusions can be summarized as follows.

(i) The stability curves reach a minimum below the value for the stability index $\alpha=-1$ (unstable) for propagation angles $a\geq 10°$, and this minimum drops as the angle increases. The presence of this minimum allows the correspondence of two different values of the perturbation parameter to the same value of the stability index α.

(ii) There exist period-doubling bifurcations from the main family. As the angle of propagation increases one obtains period-doubling bifurcations for smaller values of the perturbation parameter. This is not the case for the relativistic model where there are no bifurcations from the main family.

(iii) The number of resonances being born increases as the angle of propagation increases (with constant perturbation parameter). There also exists a critical value of the angle of propagation where this number increases immensely. In contrast, it has been found that in the relativistic case this number seems to saturate.

(iv) The stability of the MF depends on ϵ and a. It also

depends strongly upon the initial conditions. For the same values of the normalized amplitude ϵ but different initial conditions, the value of the stability index can be more than two orders of magnitude greater.

(v) There is a trend towards progressively higher absolute values of the stability index as one moves from parent to daughter bifurcating families.

As far as the energy distribution is concerned, an extremely important feature appears in the relativistic case: The regular motion is characterized by an energy band structure; the energies acquired by the accelerated electrons stay within relatively narrow bands. These characteristic energy bands widen as the angle of propagation increases. This broadening also occurs for electrons of higher initial energies. Therefore, a narrow band structure is indicative of small amplitudes and small angles of propagation. For appreciable values of the angle of propagation, a narrow band structure characterizes low initial energies. The band structure disappears completely as the amplitude increases. The threshold amplitude for band destruction decreases as the angle of propagation increases. Therefore, the energy distribution studies provide a good semiquantitative assessment of the transition to stochasticity and the accelerating field parameters, namely, the normalized amplitude and the angle of propagation with respect to the electron beam. Since the energy can be directly measured, the energy diagrams may prove a very useful tool for studying the accelerating electron dynamics a step closer towards the experimental situations. Similar arguments can be made for the nonrelativistic case as well. However, the kinetic energy is relatively very low and, because of the bounded character of motion, is distributed in a narrow region.

Finally, the precise structure of bubbles of order higher than those studied in this work is an open issue and a tedious task for future investigation.

ACKNOWLEDGMENT

We wish to thank Professor G. Contopoulos for his very constructive criticism and comments.

[1] V. Y. Davydovskii, Zh. Eksp. Teor. Fiz. **43**, 886 (1962) [Sov. Phys. JETP **16**, 629 (1963)].
[2] C. S. Roberts and S. J. Buchsbaum, Phys. Rev. A **135**, 381 (1964).
[3] S. P. Kuo and G. Schmidt, J. Appl. Phys. **58**, 3646 (1985).
[4] J. L. Vomvoridis, IEEE Trans. Nucl. Sci. **NS-28**, 3418 (1981).
[5] R. R. Sharma, L. Vlahos, and K. Papadopoulos, Astron. Astrophys. **112**, 377 (1982).
[6] P. J. Palmadesso, Phys. Fluids **15**, 2006 (1973).
[7] H. Karimabadi, C. R. Menyuk, P. Sprangle, and L. Vlahos, Astrophys. J. **316**, 462 (1987).
[8] G. R. Smith and A. N. Kaufman, Phys. Fluids **21**, 2230 (1978).
[9] D. R. Shklyar, Zh. Eksp. Teor. Fiz. **80**, 2272 (1981) [Sov. Phys. JETP **53**, 1187 (1981)].
[10] K. Akimoto and H. Karimabadi, Phys. Fluids **31**, 1505 (1988).
[11] T. Stix, *The Theory of Plasma Waves* (McGraw-Hill, New York, 1962).
[12] K. Hizanidis, Phys. Fluids B **1**, 675 (1989).
[13] K. Hizanidis, L. Vlahos, and C. Polymilis, Phys. Fluids B **1**, 682 (1989).
[14] M. Henon and C. Heiles, Astron. J. **69**, 73 (1964).
[15] B. Barbanis, Astron. J. **71**, 145 (1966).
[16] G. Contopoulos and C. Polymilis, Physica **24D**, 328 (1987).
[17] M. Henon, Ann. Astrophys. **28**, 292 (1965).
[18] G. Contopoulos, Lett. Nuovo Cimento **37**, 1491 (1983).
[19] G. Contopoulos, Physica **8D**, 142 (1983).
[20] G. Contopoulos and C. Polymilis, Phys. Rev. E **47**, 1546 (1993).